Published in final edited form as:

Nat Methods. 2015 October; 12(10): 969–974. doi:10.1038/nmeth.3536.

Wirelessly powered, fully internal optogenetics for brain, spinal and peripheral circuits in mice

Kate L Montgomery^{1,7}, Alexander J Yeh^{2,7}, John S Ho², Vivien Tsao², Shrivats Mohan Iyer¹, Logan Grosenick^{1,3}, Emily A Ferenczi^{1,3}, Yuji Tanabe², Karl Deisseroth^{1,3,4,5}, Scott L Delp^{1,6}, and Ada S Y Poon²

¹Department of Bioengineering, Stanford University, Stanford, California, USA

²Department of Electrical Engineering, Stanford University, Stanford, California, USA

³Neurosciences Program, Stanford University, Stanford, California, USA

⁴Department of Psychiatry and Behavioral Sciences, Stanford University, Stanford, California, **USA**

⁵Howard Hughes Medical Institute, Stanford University, Stanford, California, USA

⁶Department of Mechanical Engineering, Stanford University, Stanford, California, USA

Abstract

To enable sophisticated optogenetic manipulation of neural circuits throughout the nervous system with limited disruption of animal behavior, light-delivery systems beyond fiber optic tethering and large, head-mounted wireless receivers are desirable. We report the development of an easy-toconstruct, implantable wireless optogenetic device. Our smallest version (20 mg, 10 mm³) is two orders of magnitude smaller than previously reported wireless optogenetic systems, allowing the entire device to be implanted subcutaneously. With a radio-frequency (RF) power source and controller, this implant produces sufficient light power for optogenetic stimulation with minimal tissue heating (<1 °C). We show how three adaptations of the implant allow for untethered optogenetic control throughout the nervous system (brain, spinal cord and peripheral nerve endings) of behaving mice. This technology opens the door for optogenetic experiments in which animals are able to behave naturally with optogenetic manipulation of both central and peripheral targets.

Reprints and permissions information is available online at http://www.nature.com/reprints/index.html.

AUTHOR CONTRIBUTIONS

K.L.M., A.J.Y., L.G., S.M.I., K.D., S.L.D. and A.S.Y.P. conceived the project. A.J.Y., J.S.H., Y.T. and A.S.Y.P. designed, built and characterized the wireless power source and designed the receiving coil circuitry. A.J.Y., K.L.M., V.T. and A.S.Y.P. developed the wireless implants for use in the nervous system, L.G., E.A.F., K.L.M., A.J.Y. and V.T. performed brain device experiments. S.M.I. performed and analyzed c-Fos experiments. K.L.M., A.J.Y. and V.T. completed all other experiments and analysis. Experimental work was supervised by K.D., S.L.D. and A.S.Y.P. The manuscript was written by K.L.M. and A.J.Y. with contributions from all authors.

COMPETING FINANCIAL INTERESTS

The authors declare competing financial interests: details are available in the online version of the paper.

Correspondence should be addressed to: A.S.Y.P. (adapoon@stanford.edu). ⁷These authors contributed equally to this work.

Practical and effective light delivery during behavioral modulation is a key challenge in applying optogenetics to understand and control neural function. Initial solutions to this problem have relied on tethered optical fiber–based systems, in which a fiber optic is inserted into the brain of an animal ^{1–6}. Such systems exploit the stable nature of the brain-skull interface, enabling persistent optogenetic modulation of identified neural populations. These systems have been refined over the past decade, such as by allowing fiber rotation during animal movements using optical and electrical commutators² and by improving the ease of attachment and detachment⁷. These tethered systems nonetheless impose significant constraints on experimental design and interpretation, both by requiring investigators to handle and physically restrain animals to attach an optical fiber before behavioral testing and by limiting the environments in which optogenetic experiments can be performed.

Recent efforts have been made to eliminate tethers by delivering light via wireless headmounted systems^{8–14}. Researchers have developed both wirelessly powered^{8,9} and batterypowered^{10,11} devices that deliver light to the surface of the mouse brain with an LED. Deeper brain regions can also be targeted with a flexible, injectable LED system and the option to wirelessly power through a head-mountable receiver 12,13 or with a batterypowered, modular device using commercially available components¹⁴. These advances in wireless optogenetic technology have been limited by the mass and size of the devices. The reported wireless systems weigh 0.7–3 g (refs. 8,10–12,14; the mass of a mouse head is approximately 2 g), protrude several millimeters beyond the skin and cannot be left attached to the animal for prolonged periods of time. Head-mountable devices of this mass and size ultimately limit which central structures can be targeted and prohibit optogenetic control of the spinal cord¹⁵ or peripheral nervous system. Further, they hinder the animal's freedom of movement and behavior by preventing animals from entering small enclosures or engaging in normal social interactions with other mice. Yeh et al. reported the development of a small power receiver that turned on an LED in a mouse but was not used to stimulate opsinexpressing cells or target any neural structure ¹⁶. This system transferred power over a small behavioral area with pulse frequencies too variable for controlled optogenetic experiments. A recent advance in wireless powering based on coupling between a resonant RF cavity and a mouse enables self-tracking operation over a wide area¹⁷ and could be used to power smaller optogenetic devices. No fully internal device, however, has yet enabled optogenetic control of neural circuits.

Here we report the development of an easy-to-construct, fully internal device for wireless optogenetic stimulation of brain, spinal cord or peripheral nerve endings that is two orders of magnitude smaller and lighter than previously reported remotely controlled, wireless optogenetic systems. The entire stimulator, consisting of a power receiving coil, circuit and LED, is 10–25 mm³ and 20–50 mg depending on the target neural structure and can be fully implanted beneath the skin of the mouse. The small size of the stimulator allows for implantation in peripheral locations, such as limbs or spinal cord, expanding the diversity of potential stimulation targets beyond the brain. Such miniaturized wireless devices also allow animals to move more freely and do not require the animal to be handled just before experiments. The implant is built with readily available components and tools and is powered by a custom resonant cavity, which can be machined commercially, enabling

adoption by the scientific community. Using these devices, we demonstrated wireless optogenetic control of brain, spinal and peripheral circuits in mice.

RESULTS

A resonant cavity wirelessly powers implanted devices

The implant (see below) is powered and controlled using an aluminum resonant cavity (21-cm diameter, 15-cm height) with a surface lattice of hexagons (2.5-cm diameter) to couple electromagnetic energy (1.5 GHz) to the tissue of a mouse ¹⁷ (Fig. 1a, Supplementary Fig. 1 and Supplementary Data). We optimized the size, geometry and resonant frequencies of the implant and cavity for mice and did not characterize them for use in larger animals. Conventional inductive systems transfer energy through direct coupling between two coils. In our system, however, energy is localized in a mouse placed on the lattice owing to resonant excitation of a confined electromagnetic field pattern (intrinsic mode) set by the dielectric properties and physical dimensions of the mouse. Because energy is concentrated in the mouse at all positions on the lattice, the power transfer is self-tracking and efficient enough to power the wireless implant within the mouse. Unlike for radiative alternatives to the resonant cavity, such as highly directional antennas, tracking algorithms are not required here to maintain performance over the operational area.

Miniature implants emit light throughout nervous system

Owing to the strong localization of electromagnetic energy at low gigahertz frequencies, coils smaller (1.6-mm diameter) than conventional inductive systems can be used to extract power. We took advantage of this to create wireless, light-emitting implants that are much smaller (20–50 mg, 10–25 mm³ depending on the neural target) than previously reported wireless optogenetic systems (Supplementary Fig. 2).

We created three versions of the implant to target three different neural structures: the premotor cortex of the brain, dorsal horn of the spinal cord, and peripheral nerve endings of the hind paw (Fig. 1b,c and Supplementary Fig. 3). Each device can be implanted entirely under the skin. An on-board circuit, including a three-turn coil to extract power, drives a blue micro-LED to activate channelrhodopsin 2 (ChR2) (Supplementary Fig. 4a). Acrylic encapsulation of the implant resists biological degradation and electrically insulates the circuitry. We built and soldered the implants by hand using a dissecting microscope and hot plate without any specialized facilities or processes (Supplementary Fig. 4b–m).

Light power density is suitable for optogenetic applications

We adjusted light power density by varying the input power to the resonant cavity. This dependence was characterized by measuring the emitted light power from the LED as a known current was applied using wired circuitry. We estimated light power density as a function of input power to the LED (Fig. 2a). The micro-LED was efficient (emitted light power/input power = 19%) over the range of light power densities suitable for optogenetic stimulation (1–20 mW/mm²). This efficiency varies from the manufacturer's reported efficiency of the LED (58%) and is likely due to scattering and driving the LED with a nonideal voltage. Light-pulse durations as short as 100 μ s were achieved with high fidelity,

making the device suitable for the full range of temporal manipulations possible with available channel opsins (Fig. 2b).

The resonant cavity transferred relatively uniform power across its surface. To quantify this, we measured wirelessly delivered power across the lattice of the cavity using a custom probe, with similar circuitry as in the implants, in a volume of solution (0.5% saline) simulating the body of the mouse (Supplementary Fig. 5; 5.6–15.7 mW; time-averaged cavity input power of 3.2 W, 20% duty cycle). On the basis of the received power, the input power to the cavity and the measured efficiency of the LED (Fig. 2a), we estimated the expected light power density across the surface of the resonant cavity, which varied from 9.2 to 25.8 mW/mm² (Fig. 2c). Although not used in the results reported here, this power variability can be limited by using the measured reflected power at the cavity ports to regulate the power delivered to the cavity, and thus the wireless implant (Supplementary Fig. 6, Supplementary Note 1 and Supplementary Software). We also characterized the variation of light power density as a function of height above the resonant cavity up to 3 cm to allow for bedding or additional floor structures between the mouse and cavity surface (Supplementary Fig. 7 and Supplementary Note 2). Because energy is localized over the mouse's entire body, the position of the implant within the body is not important.

Efficient LEDs minimally increase temperature in vivo

The local temperature of tissues can increase at optical stimulation sites because of photon absorption and heat diffusion from the LED, which may result in tissue damage or artifactual changes in neural activity that are not optogenetically driven¹⁸. We have mitigated LED heating by using efficient LEDs that produce sufficient light power and result in minimal heating of the surrounding tissue for duty cycles up to at least 20% (20 mW/mm²), as demonstrated by *in vivo* temperature measurements in the brain. However, heating was still higher than during fiber optic–based light delivery and may cause a change in local temperature to exceed 1 °C for duty cycles near or greater than 40% (Fig. 2d,e, Supplementary Fig. 8 and Supplementary Note 3). We also observed low but consistent general whole-mouse heating, about 0.5 °C greater than control, due to absorption of RF energy from the concentrated electromagnetic field above the cavity (Supplementary Fig. 9). Normal mouse body temperature varies between 34 °C and 39 °C (ref. 19), and the electromagnetic field did not cause fluctuations outside of this temperature range.

Wireless stimulation of premotor cortex elicits circling

To demonstrate the effectiveness of the wireless optogenetic system in the brain, we stimulated the right premotor cortex of transgenic mice expressing Thy1-ChR2-EYFP as well as wild-type controls (Figs. 1b,c and 3a) to replicate the circling behavior demonstrated by Gradinaru *et al.*². We implanted the device using a standard stereotactic apparatus and a custom, disposable implantation tool made with silica fiber. We lowered the micro-LED through a craniotomy into the brain and cemented the circuit board and coil to the skull. We then broke off the implantation tool and sutured the skin over the implant such that the implant was entirely subcutaneous (Supplementary Fig. 10).

We placed mice individually in the enclosure above the resonant cavity (Fig. 3b), alternated epochs of no stimulation with 20-s epochs of optical stimulation, and measured mouse movement within the enclosure using video-tracking software. Optical stimulation of ChR2+ mice with blue light (5-ms pulse width, 20-Hz frequency, 6- to 40-mW/mm² light power density) elicited circling behavior and increased speed of locomotion (Fig. 3c-f, Supplementary Fig. 11 and Supplementary Video 1). Circling of ChR2⁺ mice, but not implanted wild-type mice, significantly increased (Fig. 3d; 0.40 ± 0.90 (mean \pm s.e.m.) turns per minute (off epochs) to 2.5 ± 0.88 turns per minute (on epochs), n = 5 ChR2⁺ mice, paired t-test, P = 0.021, effect size (Hedge's g) = 1.65; n = 3 wild-type mice, paired t-test, P = 0.57). Such circling rates are approximately equivalent (0.25 \pm 0.088 turns per minute per duty cycle) to the original demonstration² (0.26 \pm 0.032 turns per minute per duty cycle) when normalized by duty cycle. The normalized speed of ChR2+ mice, but not implanted wild-type mice, during optical stimulation was 40% higher than without (Fig. 3e,f, n = 5ChR2⁺ mice, paired t-test, P = 0.0025, effect size (Hedge's g) = 2.4; n = 3 wild-type mice, paired t-test, P = 0.18), indicating robust optogenetic activation of premotor cortex neural circuits with the wireless implant.

Stimulation of dorsal cord induces downstream activity

We and others have previously demonstrated that nerve cuffs and optical fibers can be used to control spinal cord and peripheral nerve circuits in mice and rats^{20–22}. However, these tethered devices are typically bulky and restrict animal movement. The small size of the wireless implant we have developed here allows for straightforward targeting of neural structures outside of the brain, such as the spinal cord, without affecting locomotion (Supplementary Video 2).

Using a virus carrying ChR2 or, for controls, EYFP, we transduced unmyelinated nociceptors of the sciatic nerve that project to lamina I/IIo in the spinal cord of mice (ref. 23) and then implanted wireless spinal stimulators (Figs. 1c and 4a and Supplementary Figs. 3 and 12). The overlying muscle and skin were sutured over the implant such that it was fully enclosed beneath the skin surface. We then optically stimulated the spinal cord of both ChR2+ and EYFP+ mice for 10 min (Fig. 4b; 10-ms pulse width, 10-Hz frequency, 10-mW/mm² light power density) and histologically examined the spinal cord for c-Fos expression, which is a marker of recent neural activity.

We observed higher c-Fos expression of neurons putatively downstream of lamina I/IIo nociceptor projections (Fig. 4c,d). Asymmetry of expression of c-Fos in the ipsilateral side of the spinal cord was significantly more pronounced in ChR2⁺ mice than in EYFP⁺ controls (n = 5 ChR2⁺ mice, 7 EYFP⁺ mice (two sections averaged per mouse), unpaired t-test, P = 0.02, effect size (Hedge's g) = 1.5).

Stimulation of cutaneous nociceptors at the paw is aversive

Finally, we tested whether a wireless implant in the peripheral nervous system could alter cell activity and consequently animal behavior by optogenetically activating peripheral nerve endings. We again transduced unmyelinated nociceptors of the sciatic nerve²³ and then implanted stimulation devices for peripheral nerve endings under the skin of the hindlimbs

of mice (Figs. 1c and 5a and Supplementary Fig. 3). The circuit board and coil were positioned adjacent to the triceps surae muscle group, where there is ample subcutaneous space and minimal disruption from joint rotation, and the extension was tunneled under the skin such that the LED emitted light to the cutaneous peripheral nerve endings around the heel of the paw (Fig. 5b and Supplementary Fig. 13). This implant was well tolerated by the animals (Supplementary Fig. 14 and Supplementary Note 4).

Blue light stimulation (10-ms pulse width, 10-Hz frequency, 10 mW/mm² light power density) of the peripheral nerve endings in the hind paw of ChR2+ mice with the wireless implant increased reflexive nocifensive behavior compared to EYFP+ control mice (Supplementary Fig. 15a and Supplementary Note 5; n = 4 ChR2+ mice, 4 EYFP+ mice, unpaired t-test, P = 0.03, effect size (Hedge's g) = 1.71). To confirm neural activation, we measured c-Fos expression after 10 min of optogenetic stimulation of the peripheral nerve endings with the wireless implant. Consistent with these behavioral results, we observed increased c-Fos expression in the spinal cord ipsilateral to the stimulated paw in ChR2+ mice compared to that of EYFP+ control mice, although sample sizes were small and the difference was not significant (Fig. 5c,d; n = 3 ChR2+ mice, 2 EYFP+ mice (two sections averaged per mouse), unpaired t-test, P = 0.08).

To demonstrate the utility of the wirelessly powered implants in studying freely moving behavior, we allowed mice with ChR2-expressing nociceptors to explore a two-chamber place-aversion enclosure in which one chamber was directly above the resonant cavity (Figs. 1a and 5e). Implants produced light only when the mouse entered the resonant cavity chamber with the power on. After a 10-min habituation (cavity power off), mouse location within the two chambers was measured for 15 min (cavity power off) followed by 30 min (cavity power on). Mice had a slight baseline preference for the nonresonant cavity chamber, unrelated to the RF field as this preference existed before the resonant cavity was powered (no significant baseline difference between EYFP+ and ChR2+ mice, unpaired t-test, t=0.2). The ChR2+ mice spent significantly less time in the resonant cavity chamber than the nonresonant cavity chamber compared to EYFP+ control mice (Fig. 5f,g and Supplementary Fig. 15b; t=5 ChR2+ mice, t=6 EYFP+ mice, unpaired t-test, t=0.039, effect size (Hedge's t=0.133).

DISCUSSION

The wireless optogenetic system described here permits untethered animal movement in various behavioral testing environments, and the low mass and volume of the fully internal implant will likely minimize interference with animal behavior. Furthermore, the widespread availability of the components required to build the implants and the ease of constructing the resonant cavity will enable scientists to rapidly adopt this wireless optogenetic technology.

Care should be taken when modifying this device with less efficient LEDs or when driving the blue LED with higher powers than those reported here; increased power will increase both general heating of the animal by the RF field and local tissue heating at the LED. Also, it is important to consider how light power varies as a function of device orientation and position above the resonant cavity. Although the reported system was sufficient to elicit

reliable optogenetic control of behavior, a smaller enclosure or the use of the closed-loop tracking system can reduce the variability of light power density.

Future designs will allow for sensing and power control based on measured bioelectric signals²⁴ as well as multiple light colors to match the vast array of available spectrumsensitive opsins^{25–27}. Many untried targets, including deeper regions of the brain, other peripheral nerves, nerve plexuses and ganglia^{28,29}, may now be amenable to targeting with this wireless technology with only minimal modification to the original device. Because the entire mouse body resonantly localizes energy, the device can be powered with similar efficiency even when placed deep within the body. Perhaps the most immediate enhancements to this system will be the design of resonant cavities to decrease variability in field strength, to allow for mouse behavior in differently shaped enclosures, to account for mouse behavior tests in water—which has different dielectric properties than air—and to allow for optogenetic stimulation in larger mammals, such as rats.

With very little modification of the core technology, new optogenetic experiments may now be possible, including chronic optogenetic stimulation of mice in their home cages, stimulation while navigating constricting obstacles, simultaneous stimulation of multiple, socializing animals³⁰, simultaneous stimulation of multiple neural targets in the same animal, and stimulation of deep neural targets outside of the brain—for example, branches of the vagus nerve or components of the enteric nervous system. This optogenetic system simplifies light delivery and paves the way for more natural behavior during optogenetic experiments.

ONLINE METHODS

General statistical methods

In cases where data were known to be drawn from a non-normal distribution (von Frey measures of mechanical withdrawal), nonparametric tests were used (Wilcoxon signed-rank test). Paired *t*-tests were used for the circling and speed measurements (Fig. 3), and unpaired *t*-tests were used for comparing c-Fos expression in the spinal cord (Fig. 4) and evaluating the place-aversion measurements (Fig. 5). Homoscedastic tests were used as populations had similar variances (as measured with Levene's test). All behavioral data presented were replications of small-sample pilot experiments. Measurements of c-Fos expression were performed only once owing to humane concerns (they required nociceptors to be stimulated over several minutes) but with sufficient sample size to allow for adequate statistical power. All effect sizes were expressed through Hedge's *g*. Sample sizes were estimated to be approximately 3–7 mice per group on the basis of pilot experiments, using $\alpha = 0.05$ and power $(1 - \beta) = 0.8$ and a prespecified effect size of 0.5. Actual sample sizes were sometimes higher than calculated sample sizes to account for potential exclusion of animals (see next section, "Inclusion/exclusion criteria").

Inclusion/exclusion criteria

Exclusion criteria were predetermined. Mice were excluded if the wireless implant failed to turn on (usually because of improper electrical insulation with acrylic) or, in the case of the

peripheral implant, the subcutaneous lead migrated away from the stimulation site. Mice injected with AAV6:ChR2 that failed to display pain behavior in response to externally applied transcutaneous blue light were excluded. For wireless stimulation of the spinal cord, mice were excluded from analysis if an opaque blood clot was discovered between the LED and the spinal cord during dissection of the spinal cord.

Radio-frequency powering system

An RF signal generator (Agilent, N9310A) with power amplifier (EMPOWER RF, 1119) provides energy to the two ports of the cavity. The RF signal is evenly divided by a splitter (Pasternack, PE2074). One of the output ports of the splitter is connected to a tunable phase shifter (Pasternack, PE8243) set to provide a 90° phase shift. A cavity-type phase shifter is used to minimize the insertion loss and hence minimize the axial ratio of the fields. The power amplifier is cooled using a heat sink (ABL, 173AB2000B) and fan. The gain between the output port of the signal generator and input ports at the cavity is 48 dB. The link gain is insensitive to the transverse orientation of the power receiving coil owing to the generation of circularly polarized fields from the two-port cavity.

Implant construction

The wireless implants are constructed using readily available electronic components. The device consists of two main parts. The first part is the power receiver consisting of a three-turn coil and a rectifier. The coil extracts RF energy coupled from the cavity to the mouse. The rectifier converts the RF energy into direct current, implemented by a two-stage voltage doubling circuit using Schottky diodes. All components are bonded to a circuit board made of Rogers Printed Circuit Board (PCB) material for ease of cutting. The second part is the light-delivery portion, routing the direct current to a micro-LED designed to be implanted directly at the stimulation site. For the spinal cord implant, the LED is directly attached to the bottom of the PCB. For the brain and peripheral implants, a pair of magnet wires (~250 µm in diameter) is used to route the direct current to the LED, which is attached at the tip of the wires. Except for the additional Parylene coating for chronic implants, the entire implant is constructed using benchtop tools.

Construction of the implants requires the following components: (1) Rogers 4350 PCB (Sunstone Circuits), (2) lead-free solder paste (Chip Quik, SMD291SNL), (3) light-cure acrylic (Loctite, 3554), (4) 10-nF capacitor (Murata Electronics, GRM033R61A103KA01D), (5) 10-pF capacitor (Johanson Technology, 250R05L100GV4T), (6) Schottky diode (Skyworks, SMS7630-061), (7) 34-gauge magnet wire (Belden), (8) 36-gauge magnet wire (Belden), and (9) LED chip (Cree, DA2432).

Further, it requires the following tools: (1) microscope, (2) hot plate, (3) soldering iron, (4) light source for curing acrylic, (5) tweezers, (6) blade, (7) butane torch, (8) wire cutters, (9) 1.6-mm tubing, (10) soldering wire holder, and (11) direct current power supply.

The PCB is cut to the correct size as shown (Supplementary Fig. 4b). Ample solder paste is applied on the pads of the PCB using a fine blade. Surface mount components are then placed on the pads (Supplementary Fig. 4a,c), and the PCB is heated at 250 °C for approximately 20 s using the hot plate. The power receiving coil is constructed by wrapping

34-gauge wire around appropriately sized tubing (brain and spinal cord devices, 1.6-mm diameter; peripheral device, 1.8-mm diameter) and cutting the wires with wire cutters. The outer turns of the peripheral device coil are bent 45° to compensate for the rotation of the implant along the axis of the coil. The coil is soldered to the PCB (Supplementary Fig. 4d). Light-cure acrylic is then applied to the implant in several cycles of adhesive application and cure cycles of 40 s (Supplementary Fig. 4e).

The extension is constructed from two tightly wound 36-gauge magnet wires with the end cut by a sharp blade (Supplementary Fig. 4f). For the brain implant, the LED is mounted parallel to the axis of the extension to deliver light to target regions within the brain (Fig. 1b). Thus, the exposed copper at the end of the two wires form two conductive pads for the terminals of the LED chip. For the peripheral implant, the LED is mounted perpendicular to the axis of the extension to deliver light through the skin (Supplementary Fig. 3). In this case, the coating on a 1-mm section on the sides of the wires near the tip is removed to form two conductive pads. In both cases, the twisted magnet wires are clamped vertically to a soldering wire holder. The two ends of the wires are separated by approximately 70 µm using a sharp blade (Supplementary Fig. 4g). Solder paste is applied to the two pads (Supplementary Fig. 4h), an LED chip is mounted (Supplementary Fig. 4i), and the extension is rotated horizontal to the bench surface (Supplementary Fig. 4j). A butane torch is used to melt the solder paste and bond the LED chip to the end of the extension. The extension is cut to length, and wires at the opposite end of the LED are separated and the coating is partially removed (Supplementary Fig. 4k). A direct current power supply is used to check for polarity. Once polarity is established, the extension is soldered to the pads on the bottom of the PCB (Supplementary Fig. 41). The extension can then be bent to the desired angle. Finally, light-cure acrylic is applied to the whole implant including the extension to form an insulating and biocompatible encapsulating layer for the implant (Supplementary Fig. 4m).

Various lengths can be cut to target regions of the central and peripheral nervous system. Deeper brain regions can be targeted by using a longer extension. To ensure straightness of longer extensions, the twisted wires should be pulled taut while applying and curing the acrylic coating. The extension coated with acrylic is approximately as stiff as a 120- μ m-diameter (core and cladding) silica optical fiber and is stiff enough to penetrate the brain. If stiffer extensions are desired, a Teflon-coated stainless steel wire (200 μ m in diameter) may be twisted in with the conducting wires to increase the stiffness to approximately that of a 200- μ m-diameter optical fiber, with an associated increase in the diameter of the extension.

For chronic implants, an additional 10 μ m of Parylene-C is applied to the entire exterior of the device to form a biocompatible and impermeable membrane protecting the internal electronics. Parylene-C coating application was performed by Paratronix Inc. following a priming process of treating the implant with isopropyl alcohol, deionized water, Silquest A-174NT Organo Silane, and a vacuum.

Animal test subjects and experiments

All surgical and behavioral procedures were approved by the Stanford University Administrative Panel on Lab Animal Care. C57BL/6 mice (female). Thy1-ChR2-EYFP (line

18) transgenic mice (male and female, from The Jackson Laboratory), 1–4 months old, were housed in groups of 2–5 under a 12:12 h light-dark cycle. Food and water were available *ad libitum*.

Random assignment and blinding—To evaluate circling behavior, we filtered blue light out of videos to be scored, and a blinded experimenter scored the animals for circling behavior (Fig. 3d). Speed measurements were made automatically by software without blinding (Fig. 3e,f).

When applicable, mice injected with AAV6 (ChR2 or EYFP) were randomly assigned to experimental groups within cages at the time of injection such that EYFP⁺ and ChR2⁺ mice were cage mates (Figs. 4 and 5 and Supplementary Fig. 15a). Blinding was used with histological images for cell count measurements (Figs. 4c and 5c). Place aversion was scored automatically with software without blinding (Fig. 5f,g and Supplementary Fig. 15b). Evaluations of paw withdrawal were done with blinding (Supplementary Fig. 15a and Supplementary Note 5).

Surgical procedures

General—Each mouse was anesthetized with 2–2.5% isoflurane and given 0.1 mg carprofen via subcutaneous injection, placed on a heating pad maintained at 37 °C, and allowed to reach a stable plane of anesthesia, which was periodically checked through examination of breathing rate and a toe-pinch test. The incision site was cleared of fur and sterilized with alternating applications of ethanol and Betadine solution. After surgery, the incision was sutured using 5–0 sutures, and the mouse was allowed to recover under a heated lamp.

Implantation of device for stimulation of the brain—Implantation of our wireless device for the brain is adapted from procedures for implanting cannula-based systems^{1,2}. However, unlike cannula-based systems that feature an external component for connection of an optical fiber, the wireless brain implant is fully subcutaneous with the extension passing through the skull (Fig. 3a). To allow for precise manipulation of the small wireless implant, a detachable and disposable glass implantation tool was constructed from stripped optical fiber (Thor Labs, BFH48-400), approximately 5 cm long, and attached to the wireless device with epoxy. This tool allowed the implant to sit easily in a standard cannula holder.

After inducing anesthesia, Thy1-ChR2-EYFP transgenic mice or C57BL/6 wild-type mice were placed in the stereotactic apparatus (Supplementary Fig. 10). A midline incision was made to expose the skull, and a craniotomy was performed unilaterally to target secondary motor cortex (M2) on the right side. As in cannula-based insertion surgeries, the stereotactic frame allows precise manipulation of the implant location to match predetermined coordinates. The implant was lowered to position (AP, +1.0; ML, 0.5; DV, -0.5) (ref 31) using the implantation tool held in a standard cannula holder and secured in place to the skull using blue light–curable flowable composite (Flow-It ALC Flowable Composite, Pentron). The implantation tool was then gently twisted free from the implant until the glass broke at the base, and the skin was then sutured over the top of the implant. In practice, the full surgical procedure took 30 min per animal.

Intrasciatic injection of rAAV2/6-hSyn-ChR2(H134R)-EYFP—Virus: the virus, rAAV2/6-hSyn-ChR2(H134)-EYFP, was chosen as intrasciatic injection has been shown to transduce nociceptive neurons, leading to blue light—induced pain behavior²³. A similar construct, without ChR2, was used as a control (rAAV2/6-hSyn-EYFP). The plasmid maps and DNA are available at http://stanford.edu/group/dlab/optogenetics/sequence_info.html. These plasmids were packaged as AAV6 viruses by the UNC Vector Core; the virus can be ordered at http://www.med.unc.edu/genetherapy/vectorcore. The titer was determined by a dot-blot technique to measure viral capsids.

Injection: after inducing anesthesia in a C57BL/6 mouse, we taped the mouse legs to the surgical table and made an incision at the level of the sciatic nerve in the right leg. The sciatic nerve was carefully exposed and injected using a 35-G beveled needle (Nanofil no. NF35BV-2, World Precision Instruments). Virus solution (ChR2: 2.5–4 μ l, 2.4 × 10¹³ vector genomes/ml; EYFP: 3.0 × 10¹² vector genomes/ml) was injected at 1 μ l/min, using a 25- μ l syringe (Hamilton Company) connected to a Harvard PHD syringe pump (Harvard Apparatus). Two separate injections were made into the common peroneal and tibial branches of the sciatic nerve to ensure that the nerve was filled uniformly. In practice, the full surgical procedure took 15 min per animal.

Implantation of device for stimulation of spinal cord—C57BL/6 mice were injected intrasciatically with AAV6:ChR2 or AAV6: EYFP (control) 2–4 weeks before implantation with wireless spinal cord devices. After inducing anesthesia, mice were placed in a stereotaxic frame with spinal cord adaptors to secure the vertebral column (Supplementary Fig. 12). The dorsal process of the vertebra at the L3–L4 level of the spinal cord was removed and flattened. A small, unilateral hole was drilled into the vertebra just right of the center line.

As with the brain implant, the spinal cord implant was attached to a disposable glass implantation tool, and the device was positioned with a cannula holder such that the LED was directly centered over the hole. The implant was cemented (Parkell, Metabond Quick Cement System, S380) in place before the implantation tool was removed. The muscle was sutured with absorbable suture to provide additional support for the spinal cord implant. In practice, the full surgical procedure took 60 min per animal.

Implantation of device for stimulation of peripheral nervous system—C57BL/6 mice were injected intrasciatically with AAV6: ChR2 or AAV6:EYFP (control) 2–4 weeks before implantation with wireless peripheral nervous system devices. After inducing anesthesia, we taped the mouse legs to the surgical table and made a skin incision (1 cm) superficial to the triceps surae muscle group (Supplementary Fig. 13). The skin was blunt dissected away from the muscle. It was critical that the skin was only minimally dissected away from the muscle to make just enough room for the device, as the connections between the skin and muscle prevent the device from moving after implantation. The area just proximal to the board and coil is especially important to keep intact because it will prevent the LED from migrating away from the heel. The extension was routed subcutaneously to the heel of the hind paw such that the LED pointed toward the skin. The circuit board and coil were positioned adjacent to the triceps surae muscles but not directly beneath the

incision to prevent explantation. The skin was then sutured in place. In practice, the full surgical procedure took 20 min per animal.

Light power density and efficiency of the LED

Total light power is found by driving current via wired circuitry through an acrylic-coated LED and measuring the captured light power with an optical power meter (Thorlabs, PM100D) at a distance of 5 mm from the LED. Measuring the current and voltage across the LED using a multimeter (National Instruments USB-4065) provides the input power to the LED and, in turn, the efficiency. We measured the diameter of the extension tip after acrylic coating to be 350 μ m (area: 0.096 mm²). Light power density was calculated from the total light power from the LED divided by the area of the acrylic-coated tip of the LED.

Signal fidelity at different pulse widths

Signal fidelity of the implant was measured by placing the implant above the cavity while the RF signal was modulated to provide varying pulse widths. The implant was oriented with the LED facing an amplified photodiode (Thorlabs, PDA36A) that was connected to an oscilloscope, measuring the resulting light waveforms. The waveforms were normalized to the maximum recorded voltages.

Light power density across floor of resonant cavity

It is not possible to directly measure the variation in light intensity delivered by the implant across the behavioral area owing to the nature of the wireless powering system. A photodiode for measuring light intensity placed above the cavity interferes with the power transmission between the cavity and the implant. On the other hand, it is difficult to efficiently couple light from the micro-LED to a fiber optic for light-intensity measurements at a remote site. Therefore, we inferred the light intensity based upon power delivered wirelessly to a rectifier, at varying locations along the lattice of the microwave cavity. This was measured using a custom optical power measurement probe with the same coil structure as the implant. A small container of phantom solution (0.5% saline) that simulates muscle tissue was placed at varying locations on the lattice. Five measurements were taken using the optical measurement probe for each location. These measurements were then converted to light intensities on the basis of the characterization curves for the micro-LED probe.

General heating of mouse due to RF energy

To test the heating induced by the cavity, we sequentially confined wild-type mice to the center of the resonant cavity using a ventilated tube (10-cm diameter) placed around each mouse. RF power was switched on, coupling electromagnetic energy to the mouse while a thermal imaging camera (FLIR i7) was mounted to the top of the tube. The surface temperature change of the mouse was tracked by thermal imaging every 20 s. Three mice were tested sequentially with 4-W average input power to the cavity over 8 min. As a baseline test, three mice were tested in the same setup and over the same time duration with the resonant cavity switched off.

Local tissue heating at LED

To measure the induced temperature change of the micro-LED probe, we used a fiber optic temperature measurement probe (Neoptix, T1 sensor, Reflex signal conditioner) to measure heating in deep brain structures for tissue directly adjacent to the micro-LED. The micro-LED probe and optical fiber were attached together with adhesive tape and simultaneously inserted into the brain (AP, +1.1; ML, 1.5; DV, 4.2) (ref. 31) of an anesthetized mouse, using the surgical procedure as described above. We measured brain temperature for 1 min immediately before light delivery and 2 min during light delivery (sampling frequency: 1 Hz). To deliver light, we drove current through the LED to produce a light power density of 20 mW/mm², with duty cycles of 5%, 10%, 20% and 40% (5-ms pulse width; 10-Hz, 20-Hz, 40-Hz and 80-Hz frequencies, respectively, n = 3 trials). We chose to use 20 mW/mm² because most stimulation parameters require light power densities lower than 20 mW/mm² and we expect the resulting temperature rise to be an upper bound of what researchers can expect to occur.

Figure 2d displays the temperature versus time (average of three trials; simple moving average, period of 3 s). Figure 2e displays the average of the final 30 s of light delivery.

Measurement of circling and speed of mice

Each mouse was placed individually in the resonant chamber and allowed to habituate to the environment (power off) for about 1 min. 20-s epochs of no light stimulation and blue light stimulation (5-ms pulse width, 20-Hz frequency) were alternated for a period of up to 2 min. The light power used was the lowest value to elicit circling behavior for each mouse (6–40 mW/mm²). All trials were video recorded. Following behavioral testing, mice were returned to their home cage.

Circling—To measure circling, we filtered blue light out of individual videos, and a blinded experimenter scored the videos. The number of turns (or circles) that the mouse made within a body width away from the enclosure wall was counted during each trial. Partial turns were also counted. The terminology "turns" was used in place of "circles" to avoid confusion with in-place rotational circles.

Speed—Automated video tracking (Biobserve) was used to evaluate the locomotor behavior (speed and track length) of each mouse. The change in speed from the first light-off epoch was calculated for each subsequent trial for each mouse. This change in speed was normalized by each mouse's maximum speed. Only one mouse was completely motionless during its baseline trial, which is why it is the only mouse to have a 100% change in speed.

c-Fos immunohistochemistry and quantification

Mice were injected intrasciatically with either AAV6-hSyn-ChR2-EYFP or AAV6-hSyn-EYFP. Two to four weeks following injection, the ChR2-injected mice's light sensitivity was assessed using transdermal illumination of the mouse paw with blue light. Non-expressing mice (no flinching response to blue light) were removed from the experiment. Expressing mice were implanted with either the peripheral device or spinal cord device. One to two days after implantation, the mice were habituated for 1 h in a cylindrical chamber situated above

the wireless power source. Following habituation, the power source was turned on, and mice received wireless optogenetic stimulation through the stimulator (10 Hz, 10-ms pulse width). Mice were given intermittent breaks during the stimulation. Total stimulation time was 10 min. Mice in which implants did not switch on were excluded from the experiment.

Ninety minutes after stimulation, mice were anesthetized with $100~\mu l$ intraperitoneal Beuthanasia-D and transcardially perfused with 15~ml of cold phosphate-buffered saline ($1\times PBS$), and 15~ml of 4% paraformaldehyde (PFA). The lumbar section of the spinal cord was then removed through careful dissection. If a blood clot was discovered between the implant and the spinal cord, the mouse was excluded from analysis. Spinal cords were fixed in 4% PFA overnight and then cryoprotected in 30% sucrose (in $1\times PBS$) for at least 1~d. Spinal cords were frozen in Tissue-Tek OCT using cryo-molds, cut at $20-\mu m$ thickness using a cryostat (Leica, CM3050), and mounted on Superfrost slides.

Slides were rinsed in PBS, blocked in 0.3% Triton X-100, 2% normal donkey serum (NDS), dissolved in $1 \times PBS$ for 1 h. Samples were then incubated with primary antibody solution overnight at room temperature (0.3% Triton X-100, 5% normal donkey serum (NS), 1:500 or 1:1000 rabbit anti–c-Fos (Abcam, ab53036)), dissolved in PBS. The next day, samples were rinsed in $1 \times PBS$ and incubated for 2 h with secondary antibody solutions of 1:500 donkey anti-rabbit Cy5 in $1 \times PBS$ (Jackson Laboratories, #711-175-152). Samples were then rinsed in $1 \times PBS$ and coverslipped in PVA-Dabco. Slides were stored at -20 °C until examined.

Slides were imaged using a Leica TCS SP5 confocal scanning microscope, using 10× and 20× objectives (Supplementary Note 6). For c-Fos quantification, ChR2 and EYFP slides were stained as a group and were imaged on the same day using identical gain settings for ipsilateral and contralateral regions of the spinal cord. Representative sections were imaged (two per animal), and the number of c-Fos–positive cells in the dorsal horn were counted using Fiji³². Counters were blinded to slide identity. To control for nonspecific binding, we used the difference between the number of c-Fos–positive neurons observed in the ipsilateral and contralateral dorsal horn to quantify stimulation efficacy.

Place aversion

To test whether we could affect mouse behavior upon application of noxious stimuli, we constructed a two-chamber place-aversion apparatus that incorporated an RF chamber in which the implant would turn on and optogenetically induce a pain response in the mouse specifically in one of the two chambers. The place-aversion enclosure comprised two 17.5-cm-diameter plexiglass tubes connected by an entryway and adhered to a sheet of plexiglass. The enclosure was positioned such that one chamber rested on top of the RF resonant cavity, whereas the other sat on top of a cardboard box of equivalent height. Each mouse was placed in the enclosure and allowed a 10-min exploration and habituation period to the place-aversion enclosure with all power off. Mouse place position in the chambers was then video recorded for 15 min, after which the powering resonator beneath the RF resonant cavity chamber was turned on to provide 10-Hz, 20% duty cycle stimulation to the implant for 30 min. The implant was powered only when the mouse was in the powered resonant cavity chamber. Biobserve Viewer 2 analysis of the videos provided information on the amount of time each mouse spent in each room.

Supplementary Material

Refer to Web version on PubMed Central for supplementary material.

Acknowledgments

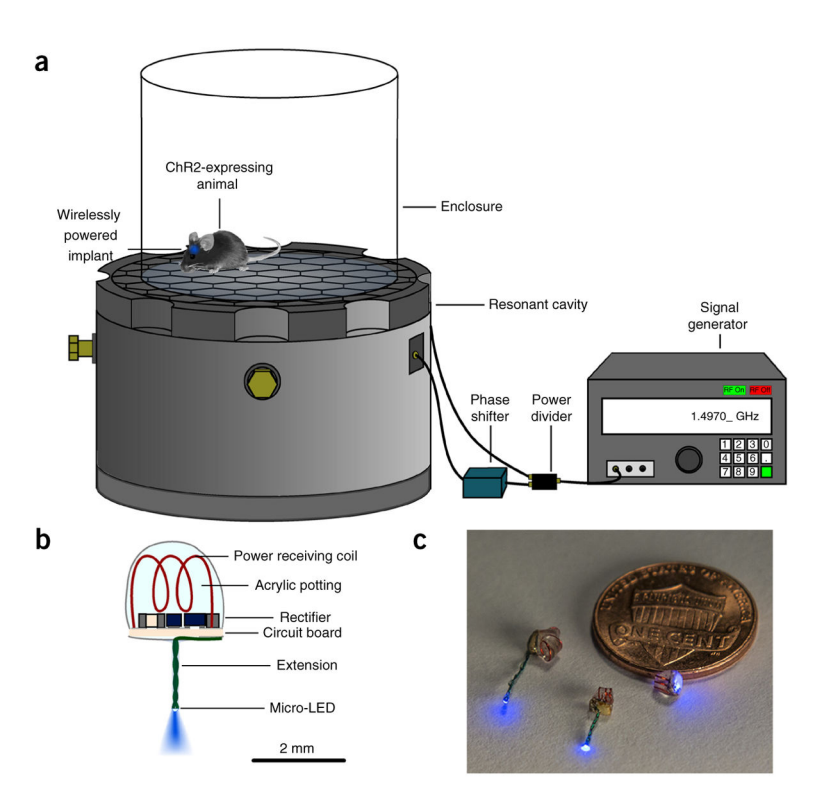
We acknowledge support from grants from the US National Institutes of Health (National Institute of Neurological Disorders and Stroke grant R01-NS080954), the US National Science Foundation (ECCS-1351687), the Stanford Bio-X NeuroVentures program and the Stanford Bio-X Interdisciplinary Initiatives Program. K.L.M. was supported by a Stanford Interdisciplinary Graduate Fellowship through the Bio-X program. We thank E. Tanabe for his advice about constructing the resonant cavity; A. Yee for assistance with photographing experimental setups; the Stanford Behavioral and Functional Neuroscience Laboratory for assistance with Rotarod experiments; and the members of the Deisseroth, Delp and Poon labs for useful discussions and assistance with experiments.

References

- Aravanis AM, et al. An optical neural interface: in vivo control of rodent motor cortex with integrated fiberoptic and optogenetic technology. J Neural Eng. 2007; 4:S143–S156. [PubMed: 17873414]
- Gradinaru V, et al. Targeting and readout strategies for fast optical neural control in vitro and in vivo. J Neurosci. 2007; 27:14231–14238. [PubMed: 18160630]
- Zhang J, et al. Integrated device for optical stimulation and spatiotemporal electrical recording of neural activity in light-sensitized brain tissue. J Neural Eng. 2009; 6:055007. [PubMed: 19721185]
- Anikeeva P, et al. Optetrode: a multichannel readout for optogenetic control in freely moving mice. Nat Neurosci. 2012; 15:163–170.
- 5. Wang J, et al. Integrated device for combined optical neuromodulation and electrical recording for chronic *in vivo* applications. J Neural Eng. 2012; 9:016001. [PubMed: 22156042]
- Warden MR, Cardin JA, Deisseroth K. Optical neural interfaces. Annu Rev Biomed Eng. 2014; 16:103–129. [PubMed: 25014785]
- 7. Klorig DC, Godwin DW. A magnetic rotary optical fiber connector for optogenetic experiments in freely moving animals. J Neurosci Methods. 2014; 227:132–139. [PubMed: 24613796]
- 8. Wentz CT, et al. A wirelessly powered and controlled device for optical neural control of freely-behaving animals. J Neural Eng. 2011; 8:046021. [PubMed: 21701058]
- 9. Kwon KY, Lee HM, Ghovanloo M, Weber A, Li W. Design, fabrication, and packaging of an integrated, wirelessly-powered optrode array for optogenetics application. Front Syst Neurosci. 2015; 9:69. [PubMed: 25999823]
- Iwai Y, Honda S, Ozeki H, Hashimoto M, Hirase H. A simple head-mountable LED device for chronic stimulation of optogenetic molecules in freely moving mice. Neurosci Res. 2011; 70:124– 127. [PubMed: 21238511]
- Hashimoto M, Hata A, Miyata T, Hirase H. Programmable wireless light-emitting diode stimulator for chronic stimulation of optogenetic molecules in freely moving mice. Neurophotonics. 2014; 1:011002. [PubMed: 26157963]
- 12. Kim TI, et al. Injectable, cellular-scale optoelectronics with applications for wireless optogenetics. Science. 2013; 340:211–216. [PubMed: 23580530]
- 13. McCall JG, et al. Fabrication and application of flexible, multimodal light-emitting devices for wireless optogenetics. Nat Protoc. 2013; 8:2413–2428. [PubMed: 24202555]
- 14. Lee ST, et al. A miniature, fiber-coupled, wireless, deep-brain optogenetic stimulator. IEEE Trans Neural Syst Rehabil Eng. 2015; 23:655–664. [PubMed: 25608307]
- 15. Carr FB, Zachariou V. Nociception and pain: lessons from optogenetics. Front Behav Neurosci. 2014; 8:69. [PubMed: 24723861]
- Yeh AJ, et al. Wirelessly powering miniature implants for optogenetic stimulation. Appl Phys Lett. 2013; 103:163701.
- 17. Ho JS, et al. Self-tracking energy transfer for neural stimulation in untethered mice. Phys Rev Appl. 2015; 4:024001.

 Yizhar O, Fenno LE, Davidson TJ, Mogri M, Deisseroth K. Optogenetics in neural systems. Neuron. 2011; 71:9–34. [PubMed: 21745635]

- 19. Gordon, CJ. Temperature Regulation in Laboratory Rodents. Cambridge Univ; New York: 1993.
- Towne C, Montgomery KL, Iyer SM, Deisseroth K, Delp SL. Optogenetic control of targeted peripheral axons in freely moving animals. PLoS ONE. 2013; 8:e72691. [PubMed: 23991144]
- 21. Caggiano V, Sur M, Bizzi E. Rostro-caudal inhibition of hindlimb movements in the spinal cord of mice. PLoS ONE. 2014; 9:e100865. [PubMed: 24963653]
- 22. Lu C, et al. Polymer fiber probes enable optical control of spinal cord and muscle function *in vivo*. Adv Funct Mater. 2014; 24:6594–6600.
- 23. Iyer SM, et al. Virally mediated optogenetic excitation and inhibition of pain in freely moving nontransgenic mice. Nat Biotechnol. 2014; 32:274–278. [PubMed: 24531797]
- 24. Nguyen TK, et al. Closed-loop optical neural stimulation based on a 32-channel low-noise recording system with online spike sorting. J Neural Eng. 2014; 11:046005. [PubMed: 24891498]
- 25. Mattis J, et al. Principles for applying optogenetic tools derived from direct comparative analysis of microbial opsins. Nat Methods. 2012; 9:159–172.
- 26. Lin JY, Knutsen PM, Muller A, Kleinfeld D, Tsien RY. ReaChR: a red-shifted variant of channelrhodopsin enables deep transcranial optogenetic excitation. Nat Neurosci. 2013; 16:1499–1508. [PubMed: 23995068]
- 27. Chuong AS, et al. Noninvasive optical inhibition with a red-shifted microbial rhodopsin. Nat Neurosci. 2014; 17:1123–1129. [PubMed: 24997763]
- 28. Birmingham K, et al. Bioelectronic medicines: a research roadmap. Nat Rev Drug Discov. 2014; 13:399–400. [PubMed: 24875080]
- 29. Williams JC, Denison T. From optogenetic technologies to neuromodulation therapies. Sci Transl Med. 2013; 5:177ps6.
- 30. Yizhar O. Optogenetic insights into social behavior function. Biol Psychiatry. 2012; 71:1075–1080. [PubMed: 22341368]
- 31. Franklin, KBJ., Paxinos, G. The Mouse Brain in Stereotaxic Coordinates. Academic Press; San Diego: 1997.
- 32. Schindelin J, et al. Fiji: an open-source platform for biological-image analysis. Nat Methods. 2012; 9:676–682. [PubMed: 22743772]



 $Figure \ 1. \ Light \ delivery \ using \ wirelessly \ powered \ and \ fully \ internal \ implants$

- (a) Diagram of light-delivery system.
- (b) Schematic of wireless implant customized for the brain. (c) Size comparison of wireless implants (left to right: peripheral nerve endings, brain, spinal cord) with a US 1-cent coin.

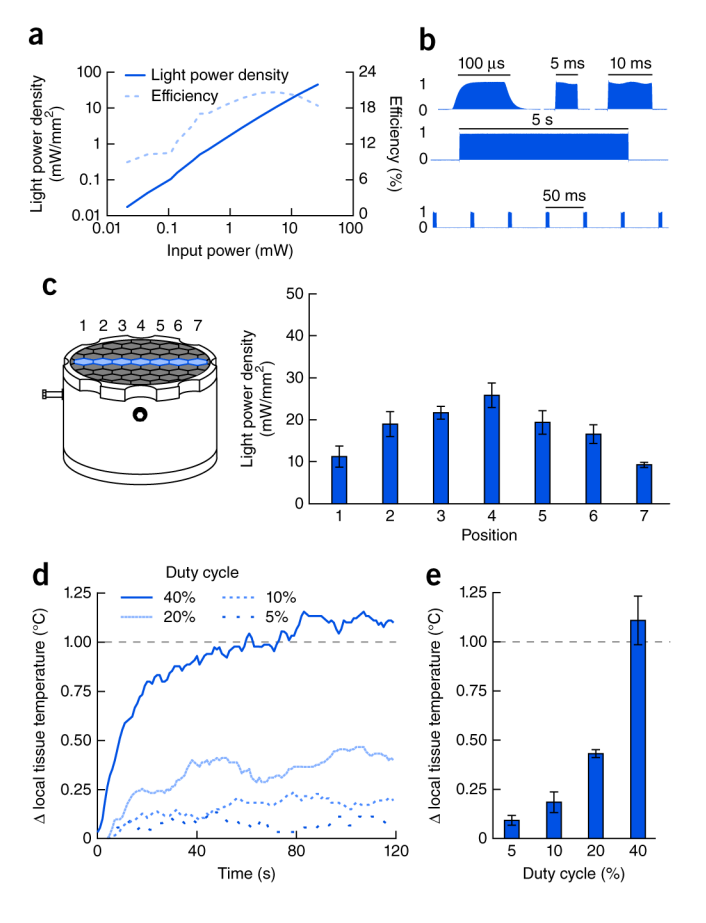


Figure 2. The implant provides light power densities and pulse characteristics suited for optogenetic stimulation without generating excessive heat. (a) Light power density and efficiency of the LED are each a function of the power supplied to the micro-LED; here, we powered the LED with a wired circuit (not wirelessly). (b) Fidelity of light output for step-function pulses of various pulse widths. Relative transient intensities (arbitrary units) for 100-μs, 5-ms, 10-ms and 5-s pulses, as well as consecutive 5-ms pulses are shown. (c) Calculated light power density across the width of the behavioral area above the resonant cavity. (d,e) Local heating of tissue directly adjacent to the LED. A wired LED probe is inserted into brain with a light power density of 20 mW/mm² at 5%, 10%, 20% and 40% duty cycles (5-ms pulse width; 10-Hz, 20-Hz, 40-Hz and 80-Hz frequencies, respectively; *n* = 3 technical trials). Dashed lines denote the temperature associated with neural damage. (d) Temperature versus time; each trace is an average of three trials. (e) Average of final 30 s of light delivery. Bar graphs show mean ± s.e.m.

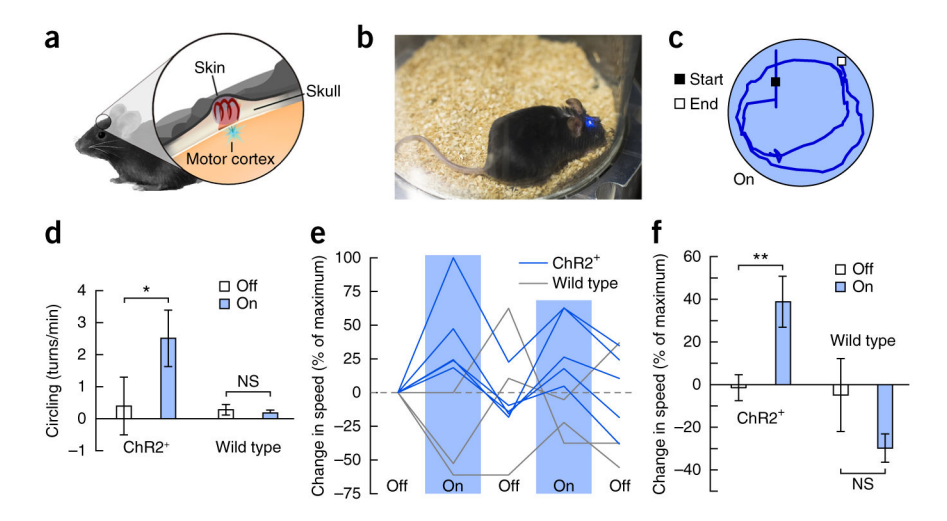


Figure 3. Wireless optogenetic stimulation of premotor cortex (M2). (a) Positioning of the device: the circuit board and coil are above the skull and below the skin; the LED at the tip of the extension is inserted into the brain directly above motor cortex. (b) Freely moving mouse with the brain implant, shown at a light power of 60 mW/mm^2 in order to be visible in the photograph. (c) Trace of mouse movement with device on for 20 s (5-ms pulse width, 20-Hz frequency); representative of 7 out of 10 such trials (mouse circling at 1 turn/min or faster). (d) Mean circling rate of ChR2+ mice, but not wild-type mice, significantly increased (0.40 turns/min to 2.5 turns/min; $n = 5 \text{ ChR2}^+$ mice, paired t-test, t= 0.021, effect size (Hedge's t= 0.65; t= 3 wild-type mice, paired t-test, t= 0.57). (e,f) Mean speed, normalized by each mouse's maximum speed, of ChR2+ but not wild-type mice was 40% greater with light stimulation than without. (e) Individual speeds of 5 ChR2+ mice and 3 wild-type mice. (f) Cohort means (t= 5 ChR2+ mice, paired t-test, t= 0.0025, effect size (Hedge's t= 2.4; t= 3 wild-type mice, paired t-test, t= 0.18). Error bars, s.e.m. NS, not significant.

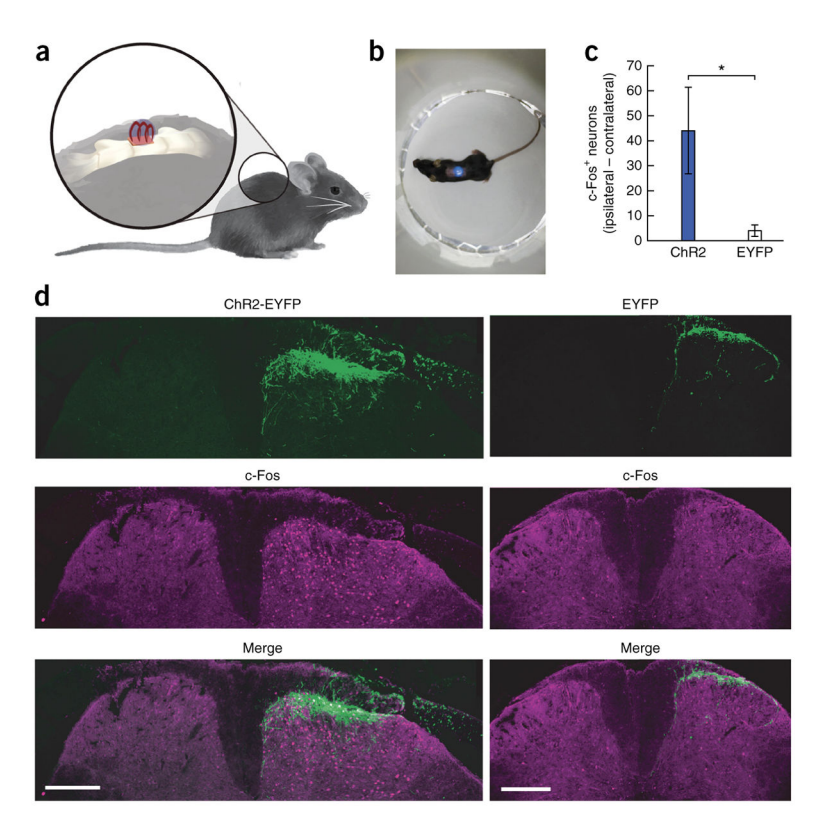


Figure 4.

The wireless implant stimulates ChR2+, unmyelinated nociceptors at the spinal cord in freely moving mice. (a) The device is implanted on the right side of the dorsal surface of the vertebra; light is delivered through a drilled hole to L3/L4 of the spinal cord. (b) Freely moving mouse with the wireless spinal cord implant, shown at a light power of 60 mW/mm² in order to be visible in the photograph. (c) Stimulation of the spinal cord was performed in awake mice (10-Hz frequency, 10-ms pulse width, 10-mW/mm² light power density). ChR2+ mice showed increased unilateral c-Fos expression during light stimulation compared to EYFP+ control mice (n = 5 ChR2+ mice, 7 EYFP+ mice (two sections averaged per mouse), unpaired t-test, *P= 0.02, effect size (Hedge's g) = 1.5). Data are shown as mean \pm s.e.m. (d) Histology images. ChR2 images are representative of 4 out of 5 ChR2+ mice (15 or more c-Fos+ neurons); EYFP images are representative of 6 out of 7 EYFP+ mice (6 or fewer c-Fos+ neurons). Scale bars, 250 µm.

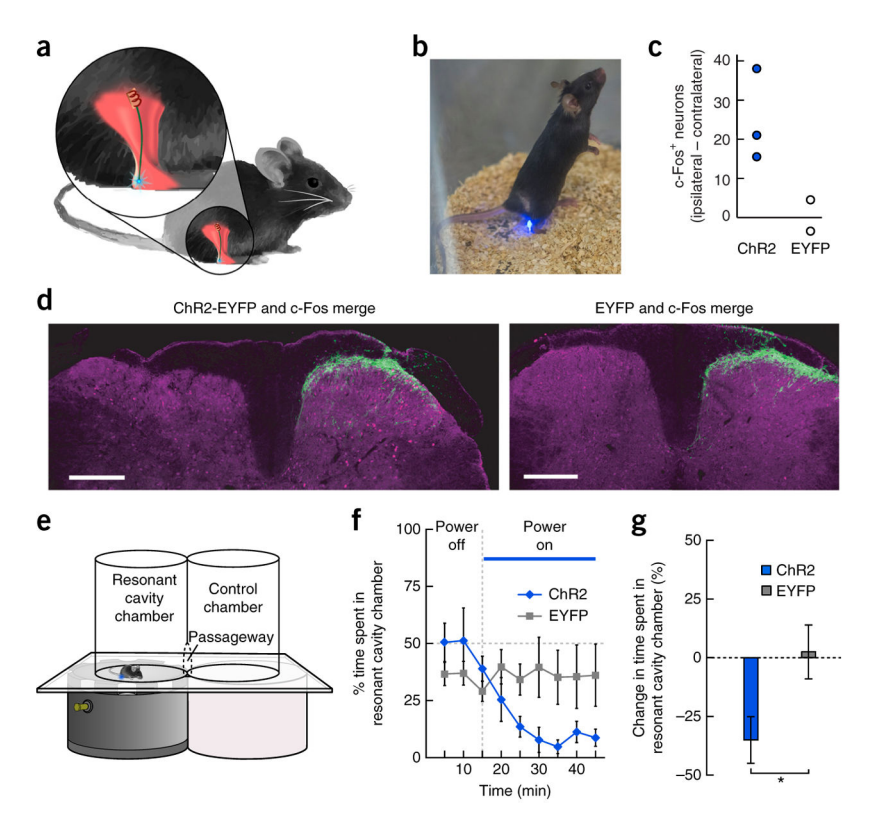


Figure 5.

The implant allows for wireless optogenetic stimulation of peripheral nerve endings. (a) Positioning of the device: the circuit board and coil are subcutaneous and adjacent to the triceps surae muscles; the micro-LED extension is subcutaneously routed to the heel. (b) Freely moving mouse with the peripheral implant (10 mW/mm²). (c) Quantification of c-Fos expression after 10 min of stimulation (10 ms, 10 Hz, 10 mW/mm²). Unilateral c-Fos expression was greater, although not significantly so, in ChR2⁺ mice than in EYFP⁺ controls $(n = 3 \text{ ChR}2^+ \text{ mice}, 2 \text{ EYFP}^+ \text{ mice})$ (two sections averaged per mouse), unpaired t-test, P =0.08). (d) Histology images, representative of all ChR2⁺ mice (15 or more c-Fos⁺ neurons; left) and EYFP+ control mice (6 or fewer c-Fos+ neurons; right). Green, EYFP; magenta, c-Fos. Scale bars, 250 µm. (e) Schematic of the place-aversion experimental setup. Chambers are above the resonant cavity and support structure, with an open passageway between them. Implants produced light only when above the powered resonant cavity. (f) Change in the percentage of time spent in the resonant cavity chamber over the course of the experiment (cohort means of 5 ChR2⁺ and 6 EYFP⁺ mice). A 'power off' period (15 min) was followed by a 'power on' period (30 min; 10-Hz frequency, 10-ms pulse width, 10-mW/mm² light power). (g) Overall change in percentage of time spent in the resonant cavity chamber, cohort mean. ChR2 mice spent 34.9% less time in the resonant cavity chamber than EYFP+ mice $(n = 5 \text{ ChR}2^+, 6 \text{ EYFP}^+ \text{ mice, unpaired } t\text{-test, } *P = 0.039, \text{ effect size (Hedge's } g) =$ 1.33). Data plotted in \mathbf{f}, \mathbf{g} as mean \pm s.e.m.